Imaging internal multiples from subsalt VSP data — Examples of target-oriented interferometry

Ivan Vasconcelos[1], Roel Snieder[2], and Brian Hornby[3]

ABSTRACT

Seismic interferometry has become a technology of growing interest for imaging borehole seismic data. We demonstrate that interferometry of internal multiples can be used to image targets above a borehole receiver array. By *internal multiples*, we refer to all types of waves that scatter multiple times inside the model. These include, for instance, interbed, intrasalt, and water-bottom multiples as well as conversions among them. We use an interferometry technique that is based on representation theorems for perturbed media and targets the reconstruction of specific primary reflections from multiply reflected waves. In this interferometry approach, we rely on shot-domain wavenumber separation to select the directions of waves arriving at a given receiver. Using a numerical walkaway (WAW) VSP experiment recorded by a subsalt borehole receiver array in the Sigsbee salt model, we use the interference of internal multiples to image the salt structure from below. In this numerical example, the interferometric image that uses internal multiples reconstructs the bottom- and top-of-salt reflectors above the receiver array as well as the subsalt sediment structure between the array and the salt. Because of the limited source summation in this interferometry example, the interferometric images show artifact reflectors within the salt body. We apply this method to a field walkaway VSP from the Gulf of Mexico. With the field data, we demonstrate that the choice of shot-domain wavenumbers in the target-oriented interferometry procedure controls the wavenumbers in the output pseudoshot gathers. Target-oriented interferometric imaging from the 20-receiver array recovers the top-of-salt reflector that is consistent with surface seismic images. We present our results with both correlation-based and deconvolution-based interferometry.

INTRODUCTION

Most exploration seismic imaging is done from surface seismic records. In areas of high structural complexity (e.g., near salt bodies), borehole seismic data can yield detailed subsurface information that cannot be obtained from surface seismic data. Hornby et al. (2005) give an example in which walkaway (WAW) VSP data acquired in a subsalt receiver array were used to image sediments below salt that were invisible using surface seismic data. Hornby et al. (2005) use standard active-shot migration methods to image the VSP data. Grech et al. (2003) give another example that uses WAW VSP data to image geologic features in a complex compressional tectonic setting in which surface seismic was compromised.

Seismic interferometry (Curtis et al., 2006; Schuster and Zhou, 2006) opens possibilities for innovative uses of borehole seismic data because it reconstructs waves that propagate between receivers as though one of them acted as a source. Hence, with interferometry, it is possible to reconstruct pseudoacquisition geometries that differ from the original physical experiments. Schuster et al. (2004) use the concept of interferometry to migrate free-surface reflections from reverse VSP data. Bakulin and Calvert (2004, 2006) use their virtual-source method to image beneath a complex overburden from borehole sensors in a horizontal well with no knowledge of the overburden model parameters. Vasconcelos and Snieder (2008a; 2008b) and Vasconcelos et al. (2007) use drill-bit noise recordings with a deconvolution interferometry method to perform broadside imaging of the San Andreas Fault at Parkfield, California. In the context of salt-flank imaging, Willis et al. (2006) present a numerical example that demonstrates that diving waves can be used for interferometric imaging of near-vertical salt reflectors. Xiao et al. (2006) present a model-based interferometric method to image-transmitted P-to-S waves that can be used for salt-flank imaging.

Here, we use internal multiples in interferometry to reconstruct primary reflections. This type of interferometry is applicable, for example, to imaging of structures above a borehole receiver array, us-

ing data from standard WAW VSP geometries. Such an interferometric imaging technique can be used to image salt and subsalt structures from borehole receivers placed beneath the target reflectors. Although no knowledge of model parameters is necessary for interferometry of internal multiples, this method relies on wavefield separation to select waves propagating in specific directions between receivers (Vasconcelos, 2007). For this reason, we refer to this method as target-oriented interferometry.

Besides being suitable for imaging features above the receiver array, target-oriented interferometry also can be tailored to image below the array. In that case, our method is analogous to the virtual-source applications of Bakulin and Calvert (2006) and of Mehta et al. (2007a). Bakulin and Calvert (2006) rely on isolation of a window around the direct arrival to separate downgoing from upgoing waves. Mehta et al. (2007a) perform a similar wavefield separation using dual-wavefield summation.

Our wavefield-separation procedure selects the directions of waves coming in to receivers according to their shot-domain wavenumbers. We rely on interference of upgoing primaries (and multiples) with downgoing internal multiples to reconstruct downgoing single scattered waves. These waves then can be used to image salt features from subsalt borehole arrays. To perform the interferometry of internal multiples, we rely on the two-way representation theorems for perturbed media derived by Vasconcelos (2007).

Other authors have proposed imaging from multiples in different contexts than the one presented here. Weglein et al. (2003) and Weglein et al. (2006) propose model-independent imaging based on an inverse-scattering-series approach. Berkhout and Verschuur (2006) compare the convolution-based multiple-elimination methods (surface-related multiple-elimination, or SRME) to crosscorrelation interferometry and propose a weighted crosscorrelation method to construct primary reflections from surface-related multiples. Hargreaves (2006) uses a similar approach to that of Berkhout and Verschuur (2006) to provide a field-data example of imaging from multiples in a shallow-water environment. Although these methods are not restricted to processing of surface seismic data, they are not designed for targeting specific arrivals or portions of the image space. This is one objective of the interferometry method we describe here. Furthermore, the Berkhout and Verschuur (2006) and Hargreaves

(2006) methods focus on imaging of surface-related multiples, whereas we focus on imaging with internal multiples.

First we use the representation theorems of Vasconcelos (2007) to describe how to manipulate recorded wavefields to generate interferometric data that target specific arrivals. Throughout the description, we give conceptual examples that apply target-oriented interferometry to imaging above and below the receiver array. Next we use the Sigsbee salt model to create a numerical subsalt WAW VSP experiment. With these synthetic data, we compare images from target-oriented interferometry with those from interferometry of the full recorded wavefields. We use internal multiples in imaging subsalt features from field WAW VSP data acquired in the Gulf of Mexico. We use the field data to give a detailed account of the effect of target-oriented interferometry in pseudoshot gathers and in the context of correlation-based and deconvolution-based (Vasconcelos and Snieder, 2008a) interferometry.

THE METHOD OF TARGET-ORIENTED INTERFEROMETRY

Retrieving desired scattered waves

This section describes how to use interferometry to target the illumination of specific regions in the subsurface. We decompose the recorded data in the frequency domain as (Vasconcelos, 2007)

$$u(\mathbf{r}_A, \mathbf{s}, \omega) = W(\mathbf{s}, \omega)[G_0(\mathbf{r}_A, \mathbf{s}, \omega) + G_S(\mathbf{r}_A, \mathbf{s}, \omega)], \quad (1)$$

where $\mathbf{s}$ and $\mathbf{r}_A$ are source and receiver locations, respectively, and ω is the angular frequency. The recorded data u are given by the superposition of the unperturbed impulse response G_0 (e.g., the incident energy at the pseudosource) and its perturbation G_S (e.g., the target scattered-wave response arriving at the receiver) (Vasconcelos, 2007). The function $W(\mathbf{s}, \omega)$ describes the excitation at $\mathbf{s}$.

Here, we assume that the medium perturbations that give rise to G_S are localized within a volume $\mathbb{P}$ (Figure 1). To generate interferometric data (Lobkis and Weaver, 2001; Wapenaar et al., 2004; Draganov et al., 2006), we crosscorrelate the data measured at $\mathbf{r}_A$ (equation 1) with that recorded at $\mathbf{r}_B$ and integrate over the sources $\mathbf{s}$, which give (e.g., Curtis et al., 2006; Larose et al., 2006)

a) **b)**

Figure 1. Geometry of the perturbation approach to target-oriented interferometric imaging. A large volume is bounded by the surface Σ that contains medium perturbations restricted to volume $\mathbb{P}$ (gray-shaded areas). Dashed lines denote closed surfaces. In (a) and (b), u_0 are unperturbed wavefields, whereas u_S are wavefield perturbations caused by scattering within volume $\mathbb{P}$. Solid lines illustrate stationary wave paths. Triangles represent two receivers at $\mathbf{r}_A$ and $\mathbf{r}_B$. The gray triangle denotes the receiver that acts as a pseudosource in the interferometric experiments. In (a) (scenario 1), we rely on waves excited by sources over surface σ_1 (solid black line). In (b) (scenario 2), interferometry targets the reconstruction of upgoing scattered waves from below the receivers. In this case, we consider only waves generated by sources on surface σ_2.

$$\oint_\Sigma u(\mathbf{r}_A, \mathbf{s}, \omega) u^*(\mathbf{r}_B, \mathbf{s}, \omega) d\mathbf{s}$$

$$= \langle |W(\mathbf{s}, \omega)|^2 \rangle [G(\mathbf{r}_A, \mathbf{r}_B, \omega) + G^*(\mathbf{r}_A, \mathbf{r}_B, \omega)], \quad (2)$$

when the integration is done over a closed surface Σ, as Figure 1 illustrates. According to this equation, interferometry reconstructs $G(\mathbf{r}_A, \mathbf{r}_B, \omega)$ (and its anticausal version), which is the response measured at $\mathbf{r}_A$ as though the source were at $\mathbf{r}_B$ (Wapenaar et al., 2004; Bakulin and Calvert, 2004). Note that G in equation 2 is the perturbed impulse response given by $G = G_0 + G_S$ (equation 1).

Equation 2 is valid for arbitrarily heterogeneous media. The objective of our experiments is to image only G_S, the waves scattered within the perturbation volume P (Figure 1). The recovered response $G(\mathbf{r}_A, \mathbf{r}_B, \omega)$ in equation 2 includes those waves. Because the pseudosource at $\mathbf{r}_A$ in equation 2 radiates energy in all directions, directly separating G_S from G in the right side of equation 2 might not be
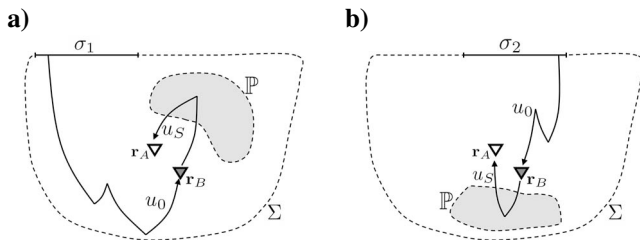
straightforward because waves in G_0 and G_S can have similar apparent wavenumbers, i.e., it is difficult to determine whether an arrival comes from above or below the array. This is a common problem, for example, for free-surface multiple suppression in ocean-bottom-cable (OBC) data (Mehta et al., 2007a).

To overcome this problem with borehole seismic data, we propose a method that separates wavefields before interferometry. This produces pseudosources that radiate most of the energy in a range of preferential directions. These directions are chosen so that the resultant interferometric data reconstruct only the desired waves G_S.

Another form of interferometry that targets extraction of the wavefield perturbation $G_S(\mathbf{r}_A, \mathbf{r}_B, \omega)$ measured at $\mathbf{r}_A$ and excited by a pseudosource at $\mathbf{r}_B$ is

$$\int_{\sigma_i} u_S(\mathbf{r}_A, \mathbf{s}, \omega) u_0^*(\mathbf{r}_B, \mathbf{s}, \omega) d\mathbf{s} \approx \langle |W(\mathbf{s}, \omega)|^2 \rangle G_S(\mathbf{r}_A, \mathbf{r}_B, \omega);$$

$$(3)$$

(Vasconcelos, 2007), where integration over sources no longer is conducted over the closed surface Σ but rather over a part of it, denoted by σ_i, a chosen segment of Σ (σ_1 or σ_2 in Figure 1). Vasconcelos (2007) provides details regarding the derivation of equation 3. First, the integrand on the left side of equation 2 contains the correlation of perturbed wavefields u, whereas the integrand in equation 3 correlates the unperturbed wavefield $u_0(\mathbf{r}_B, \mathbf{s}, \omega)$ with wavefield perturbation $u_S(\mathbf{r}_A, \mathbf{s}, \omega)$. Wavefield $u_0(\mathbf{r}_B, \mathbf{s}, \omega)$, wavefield perturbation $u_S(\mathbf{r}_A, \mathbf{s}, \omega)$, and retrieved quantity $G_S(\mathbf{r}_A, \mathbf{r}_B, \omega)$ represent different types of waves for each chosen application. Below, we describe how to generate $u_0(\mathbf{r}_B, \mathbf{s}, \omega)$ and $u_S(\mathbf{r}_A, \mathbf{s}, \omega)$ by shot-domain wavefield separation for different interferometric applications.

Although data from interferometry contain the average source power spectra (see equations 2 and 3), in principle, the effect of the excitation function can be removed from reconstructed data. Estimates of the power spectra of the source function can be used to extract the impulse response from interferometry (Wapenaar and Fokkema, 2006; Mehta et al., 2007a).

Interferometry by deconvolution (Vasconcelos and Snieder, 2008a, 2008b) is an option for reconstructing an interferometric impulse response when estimates of the source power spectra are not available. Because deconvolution is given by

$$D_{AB} = \frac{u(\mathbf{r}_A, \mathbf{s}, \omega)}{u(\mathbf{r}_B, \mathbf{s}, \omega)} = \frac{u(\mathbf{r}_A, \mathbf{s}, \omega) u^*(\mathbf{r}_B, \mathbf{s}, \omega)}{|u(\mathbf{r}_B, \mathbf{s}, \omega)|^2}$$

$$= \frac{G(\mathbf{r}_A, \mathbf{s}, \omega) G^*(\mathbf{r}_B, \mathbf{s}, \omega)}{|G(\mathbf{r}_B, \mathbf{s}, \omega)|^2}; \qquad (4)$$

the source wavelet $W(\mathbf{s}, \omega)$ (equation 1) cancels. Using equation 4, deconvolution interferometry (Vasconcelos and Snieder, 2008a) yields

$$\oint_{\Sigma} D_{AB} d\mathbf{s} = \oint_{\Sigma} \frac{G(\mathbf{r}_A, \mathbf{s}, \omega) G^*(\mathbf{r}_B, \mathbf{s}, \omega)}{|G(\mathbf{r}_B, \mathbf{s}, \omega)|^2} d\mathbf{s}, \qquad (5)$$

Vasconcelos and Snieder (2008a) show that equation 5 reconstructs (1) causal and anticausal G_0 (from the first integral), (2) only causal G_S, and (3) spurious arrivals that are intrinsic to deconvolution interferometry of full recorded data. See Vasconcelos and Snieder (2008a) for a detailed discussion on single-channel deconvolution interferometry of acoustic wavefields.

When wavefield-separation methods are available (see below), allowing us to distinguish u_0 from u_S (equation 1), interferometry by deconvolution also can be represented by

$$\int_{\sigma_i} D'_{AB} d\mathbf{s} = \int_{\sigma_i} \frac{G_S(\mathbf{r}_A, \mathbf{s}, \omega) G_0^*(\mathbf{r}_B, \mathbf{s}, \omega)}{|G_0(\mathbf{r}_B, \mathbf{s}, \omega)|^2} d\mathbf{s}, \qquad (6)$$

(Vasconcelos and Snieder, 2008a), where

$$D'_{AB} = \frac{u_S(\mathbf{r}_A, \mathbf{s}, \omega)}{u_0(\mathbf{r}_B, \mathbf{s}, \omega)} = \frac{G_S(\mathbf{r}_A, \mathbf{s}, \omega)}{G_0(\mathbf{r}_B, \mathbf{s}, \omega)}. \qquad (7)$$

This form of deconvolution interferometry yields $G_S(\mathbf{r}_A, \mathbf{r}_B, \omega)$ (as does the correlation method in equation 3) but without the source power-spectra average $\langle |W(\mathbf{s}, \omega)|^2 \rangle$.

In particular, deconvolution interferometry can be more effective than its correlation-based counterpart in reconstructing impulsive pseudosources when the input excitation consists of a complicated, unknown waveform (Vasconcelos, 2007; Vasconcelos and Snieder, 2008a). This can be the case when excitation comprises complicated waves coming from the earth's subsurface (Snieder and Şafak, 2006; Mehta et al., 2007b). Note, for example, that the excitation recorded by $\mathbf{r}_B$ in Figure 1a consists of a superposition of primaries and, to a lesser extent, of higher-order multiples. Consequently, the signal corresponding to this excitation could be a complicated, incoherent function. Here, apart from using correlation interferometry, we also rely on a deconvolution interferometry method (e.g., Vasconcelos and Snieder, 2008a) to create impulsive images from our data examples.

Wavefield separation and applications

The unperturbed wavefield $u_0(\mathbf{r}_B, \mathbf{s}, \omega)$ and the perturbation $u_S(\mathbf{r}_A, \mathbf{s}, \omega)$ are obtained from the recorded data $u(\mathbf{r}_B, \mathbf{s}, \omega)$ perturbation $u(\mathbf{r}_A, \mathbf{s}, \omega)$ by using wavefield separation. This separation is done in the shot domain, i.e., for a fixed source $\mathbf{s}$ and varying receiver position $\mathbf{r}$, according to

$$u_0(\mathbf{r}, \mathbf{s}, \omega) = \int \mathcal{H}_B(\mathbf{k_r}) u(\mathbf{k_r}, \mathbf{s}, \omega) e^{i\mathbf{rk_r}} d\mathbf{k_r} \qquad (8)$$

and

$$u_S(\mathbf{r}, \mathbf{s}, \omega) = \int \mathcal{H}_A(\mathbf{k_r}) u(\mathbf{k_r}, \mathbf{s}, \omega) e^{i\mathbf{rk_r}} d\mathbf{k_r}, \qquad (9)$$

where $\mathbf{k_r}$ is the apparent shot-domain wavenumber vector, i.e., wavenumbers measured directly from the recorded shot gathers. The integrals in equations 8 and 9 represent a multidimensional inverse Fourier transform that maps $\mathbf{k_r} \mapsto \mathbf{r}$. The functions $\mathcal{H}_B$ and $\mathcal{H}_A$ are band-pass filters in the wavenumber domain that select which portion of $\mathbf{k_r}$ is kept for interferometry.

This filtering translates into selecting waves recorded by the receiver array with specific incoming directions. These directions are set by either $\mathcal{H}_B$ or $\mathcal{H}_A$ (equation 8 or 9). When all desired shots on σ (equation 3) have been filtered, the resultant data from equations 8 and 9 are sorted into the receiver gathers $u_0(\mathbf{r}_B, \mathbf{s}, \omega)$ and $u_S(\mathbf{r}_A, \mathbf{s}, \omega)$, respectively. Because $\mathcal{H}_B$ sets the direction of incoming energy at the receiver that acts as a pseudosource at $\mathbf{r}_B$ (equation 3), it determines the directions over which the pseudosource radiates energy. The filter $\mathcal{H}_A$ defines the directions from which energy is recorded at the receiver $\mathbf{r}_A$.

Along with the choice of filters $\mathcal{H}_A$ and $\mathcal{H}_B$, the choice of which sources are used should be taken into account, (σ_1 or σ_2; Figure 1) also is important for proper reconstruction of the desired waves in $G_S(\mathbf{r}_A, \mathbf{r}_B, \omega)$ (our equation 3; Vasconcelos, 2007). Below, we provide examples of choices for $\mathcal{H}_A$ and $\mathcal{H}_B$ and for sources for two specific scenarios (Figure 1).

In scenario 1 (Figure 1a), the portion $\mathbb{P}$ of the medium that we want to image is above the receivers. To image perturbations within $\mathbb{P}$ in Figure 1a, we rely on upgoing scattered waves u_0 that generate downgoing wavefield perturbations u_S. The arrows in Figure 1a show an example of these arrivals.

Scenario 2 (Figure 1b) consists of a target perturbation volume $\mathbb{P}$ that is below the receivers. In this case, for interferometry, one may use downgoing unperturbed waves u_0 and upgoing wavefield perturbations u_S. Scenario 2 is the same as in earlier applications of the virtual-source method (Bakulin and Calvert, 2006; Mehta et al., 2007a).

In the example in Figure 1a, interferometry recovers the desired perturbations $u_S(\mathbf{r}_A, \mathbf{r}_B, \omega)$ from sources over σ_1, whereas in Figure 1b, it recovers the perturbations from sources over σ_2. It is not necessary to know the precise shot coordinates as long as the waves radiated by the shots come from surface segment σ_i. We chose segment σ_i on the basis of the relative position of the receivers and the portion of

the surface we wish to image (volume $\mathbb{P}$). For example, sources over σ_1 excite direct waves that propagate downward and rightward in Figure 1a and, when reflected in the unperturbed medium, are recorded as upgoing waves u_0 in the figure. In Figure 1b, the sources over σ_2 radiate energy directly down toward the receivers and thus are suitable for reconstructing the desired scattered perturbations from interferometry (see also Bakulin and Calvert, 2006, and Mehta et al., 2007a).

Figure 2a describes the wavefield separation necessary to target the imaging of scatterers above the receiver array, as in scenario 1 (Figure 1a). This is a visual description of $\mathcal{H}_B$ and $\mathcal{H}_A$ in equations 8 and 9 (see also Table 1). In this case, keeping the negative shot-domain wavenumbers at $\mathbf{r}_B$ (left side of Figure 2a) defines $u_0(\mathbf{r}_B, \mathbf{s}, \omega)$ (equations 3 and 8), which contains mostly upgoing incoming waves. This ensures that the pseudosource at $\mathbf{r}_B$ (equation 3) radiates mostly upgoing energy.

For the receivers that record the interferometric data, represented by $\mathbf{r}_A$, the choice of incoming wave direction depends on the relative positioning between a given receiver and the pseudosource at $\mathbf{r}_B$. If the receiver is above the pseudosource (top right image, Figure 2a), then waves with $k_r < 0$ give $u_S(\mathbf{r}_A, \mathbf{s}, \omega)$ (equations 3 and 9). For $\mathbf{r}_A$ below $\mathbf{r}_B$, we use waves with $k_r > 0$ to extract $u_S(\mathbf{r}_A, \mathbf{s}, \omega)$. The interferometry of wavefields separated according to Figure 2a generates a pseudoshot gather that radiates energy toward the top right corner of the model (Table 1).

To image below the receiver array, as in scenario 2 (Figure 1b), wavefield separation can be done according to Figure 2b (see also Table 1). For the pseudosource at $\mathbf{r}_B$, we select downgoing incoming waves $u_0(\mathbf{r}_B, \mathbf{s}, \omega)$ that are excited by the sources over σ_2 (Figure 1b) by preserving arrivals with $k_r > 0$ (left image, Figure 2b). In the interferometry experiment, keeping waves that have $k_r < 0$ at the recording receivers yields $u_S(\mathbf{r}_A, \mathbf{s}, \omega)$ (right image, Figure 2b). Table 1 relates the image in Figure 2b with the filters $\mathcal{H}_A$ and $\mathcal{H}_B$ in equations 8 and 9. After wavefield separation as in Figure 2b, we obtain pseudoshot gathers that radiate energy downward (Table 1).

As mentioned above, the case of Figure 1b also is the objective of the virtual-source method (Bakulin and Calvert, 2006; Mehta et al., 2007a). Those studies rely on different wavefield-separation techniques than ours. Bakulin and Calvert (2006) window the data in the time-domain receiver gathers, using a small window containing the direct arrival as u_0 and using the remainder of the data as u_S. Along with windowing, Mehta et al. (2007a) use a method based on summation of vertical and hydrophone components in four-component OBC data to separate downgoing from upgoing wavefields and treat them as u_0 and u_S, respectively.
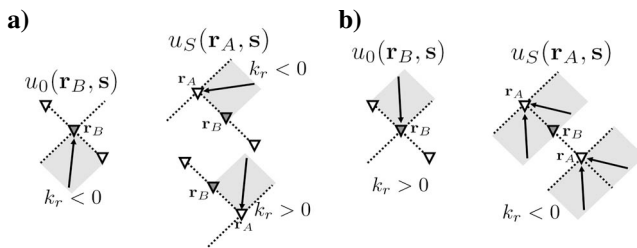

Figure 2. Examples of wavefield separation for target-oriented interferometry. Wavefield u_0 and perturbation u_S are extracted from recorded perturbed wavefield u using wavefield separation (equations 8 and 9). Wavefield separation is implemented by wavenumber filtering (e.g., f-k filtering) in the shot domain. Triangles represent receivers. Gray triangles indicate the receiver that acts as a pseudosource (at $\mathbf{r}_B$). Arrows indicate directions of waves arriving at the receivers. The directions parallel and perpendicular to the receiver line define a coordinate frame indicated by dashed lines. In this coordinate frame, $\mathbf{k}_r = (k_r, 0, 0)$, or simply k_r, is the apparent shot-domain wavenumber of a given recorded wave. Panel (a) illustrates separation of wavefields necessary for target-oriented interferometric imaging in the context of scenario 1 (Figure 1a), whereas wavefield separation in (b) is designed for the imaging experiment in scenario 2 (Figure 1b). The right sides of (a) and (b) represent a choice for filter $\mathcal{H}_B$ in equation 8, and the left sides are choices for $\mathcal{H}_A$ in equation 9 (also see Table 1).

Table 1. Summary of required elements for target-oriented interferometry for scenarios 1 and 2.[4]

	u_0	u_S	$\mathcal{H}_A$	$\mathcal{H}_B$	Sources	Radiation
Scenario 1	Upgoing (e.g., primaries)	Downgoing (e.g., multiples)	$k_r > 0$: $\mathbf{r}_A$ below $\mathbf{r}_B$ $k_r < 0$: $\mathbf{r}_A$ above $\mathbf{r}_B$	$k_r < 0$	σ_1	↗
Scenario 2	Downgoing (e.g., direct-wave)	Upgoing (e.g., primaries)	$k_r < 0$	$k_r > 0$	σ_2	↓

[4]Column-heading meanings are as denoted in Figures 1 and 2. The "Radiation" column shows the direction in which the pseudosource radiates energy. Arrows are oriented with respect to the receiver arrays denoted in Figure 2.

NUMERICAL EXAMPLE

We present an example that consists of a subsalt WAW VSP numerical experiment that uses the Sigsbee velocity model. This example uses the subsalt WAW VSP data to image the Sigsbee salt canopy from below, using interference of internal multiples, analogous to the example in Figure 1. Figure 3 illustrates the model and the experiment. The experiment simulates the recording of shots placed 500 ft (152 m) deep and recorded at 100 evenly spaced receivers in a deviated borehole (Figure 3). The first receiver is at $x = 48,000$ ft (14,630 m) and is 16,000 ft (4876 m) deep. The last receiver is at 52,950 ft (16139 m) and is 20,950 ft (6385 m) deep. The shots begin at $x = 10,000$ ft (304 m) with a shot interval of 125 ft (38 m). The source waveform is a Ricker wavelet with 12-Hz peak frequency. In our experiments, we consider shots placed from $x = 10,000$ ft (304 m) to $x = 53,500$ ft (16,306 m, corresponding to surface σ_1 in Figure 1a).

Figure 4 shows interferometric images that use the full recorded data (no wavefield separation). Table 2 summarizes the processing that leads to Figures 4 and 5 (see discussion below). The imaging in these examples was done by wavefield extrapolation in a slant coordinate system that conforms to the receiver array. Wavefield extrapolation was done using the split-step Fourier phase-shift-plus-interpolation method (Kessinger, 1992). Figure 4a was generated using crosscorrelation interferometry, whereas Figure 4b was obtained from deconvolution interferometry after source summation (Vasconcelos and Snieder, 2008a). The images in Figure 4 show an accurate reconstruction of the salt canopy, especially toward the right side of the model, where the salt flanks dip. Above the receiver array, the imaged salt is characterized by reflectors that are weak compared with the dipping salt flanks. The images of the sediments between the salt and the receiver array are distorted and do not reproduce the horizontal bedding of the model (Figure 3).

After applying the target-oriented interferometry method that is based on wavefield separation outlined in Table 2 (see also Figure 2a), we obtain the images in Figure 5. We adapt the wavefield separation in Figure 2a to also include positive numbers recorded at $\mathbf{r}_A$ above $\mathbf{r}_B$ (compare the $\mathcal{H}_A$ and "Radiation" columns in Tables 1 and 2). This ensures that the array in the interferometric experiment also records waves that come from directly above the receivers, as indicated by the "Radiation" column in Table 2.

Although the original source-and-receiver geometry in Figures 4 and 5 is the same, the portion of the model illuminated by these two sets of images is substantially different. As discussed in the section titled "The Method of Target-oriented Interferometry," pseudosources reconstructed by target-oriented interferometry are designed to radiate energy upward (Table 2). Hence, the images in Figure 5 illuminate the model predominantly in the area above the receiver array. These images show bright reflectors at the bottom and top of salt above the array, which appear as dim reflectors in the Figure 5 images.

Figure 5 shows that the target-oriented interferometric images recover the structure of the subsalt sediments that are not seen in Figure 4. The reflector that corresponds to the dipping top salt (right images, Figure 4) is absent from the target-oriented interferometric images in Figure 5. That is because in Figure 4, it was imaged from reflections reconstructed from diving waves that arrive at the receiver
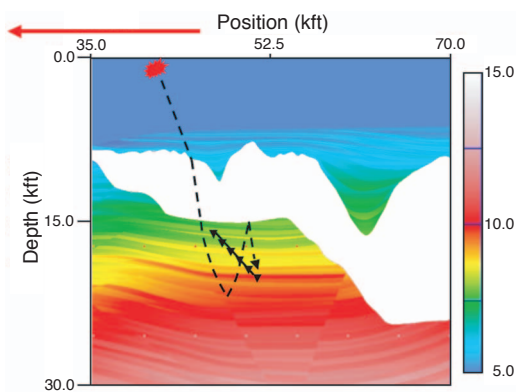

Figure 3. Geometry of the numerical experiment with the Sigsbee model. The figure displays the model structure, color-coded by acoustic wave speed in kft/s. A receiver array with 100 sensors is set beneath the salt body in a 45°-inclined borehole (solid line with triangles). Shots are placed in a horizontal line 500 ft (152 m) below the water surface and extend laterally toward the left side of the receiver array (red arrow). Interferometry is used to image the salt with the receiver array by reconstructing downgoing primary reflections that propagate between the receivers from internal multiples. The dashed black arrow illustrates the path of one such multiple.
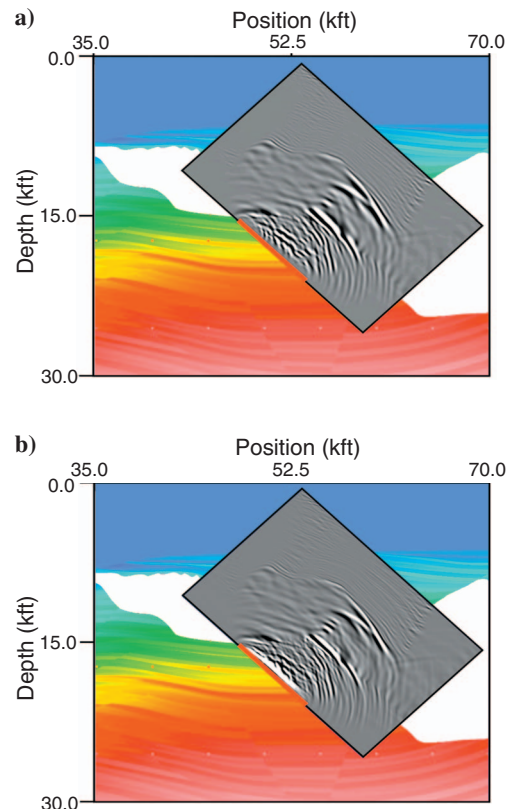

Figure 4. Images obtained from interferometry of data acquired in the numerical experiment (Figure 3). The grayscale images are superposed over the velocity model from (Figure 3). The images are based on (a) crosscorrelation interferometry and (b) deconvolution interferometry. We use the full wavefield recorded at the receivers to reconstruct the interferometric shot gathers from which these images are obtained.

Table 2. Summary of the interferometric procedures that produce the images in Figures 4 and 5.[5]

	u_0	u_S	$\mathcal{H}_A$	$\mathcal{H}_B$	Sources	Method	Radiation
Figure 4a	Not separated	Not separated	Not applicable	Not applicable	All	Correlation (equation 2)	Not controlled*
Figure 4b	Not separated	Not separated	Not applicable	Not applicable	All	Deconvolution (equation 5)	Not controlled*
Figure 5a	Upgoing (e.g., primaries)	Downgoing (e.g., multiples)	$k_r>0$; $\mathbf{r}_A$ below $\mathbf{r}_B$ All k_r; $\mathbf{r}_A$ above $\mathbf{r}_B$	$k_r<0$	Above and to left of array	Correlation (equation 3)	↑ + ↗
Figure 5b	Upgoing (e.g., primaries)	Downgoing (e.g., multiples)	$k_r>0$; $\mathbf{r}_A$ below $\mathbf{r}_B$ allk_r; $\mathbf{r}_A$ above $\mathbf{r}_B$	$k_r<0$	Above and to left of array	Deconvolution (equation 6)	↑ + ↗

[5]Column-heading meanings are as for Table 1. The additional "Method" column shows the kind of interferometry used. The radiation arrows here are oriented with respect to the Figure 3 model. The asterisk indicates that the pseudosource radiation is controlled not by processing method but by acquisition geometry and model parameters.
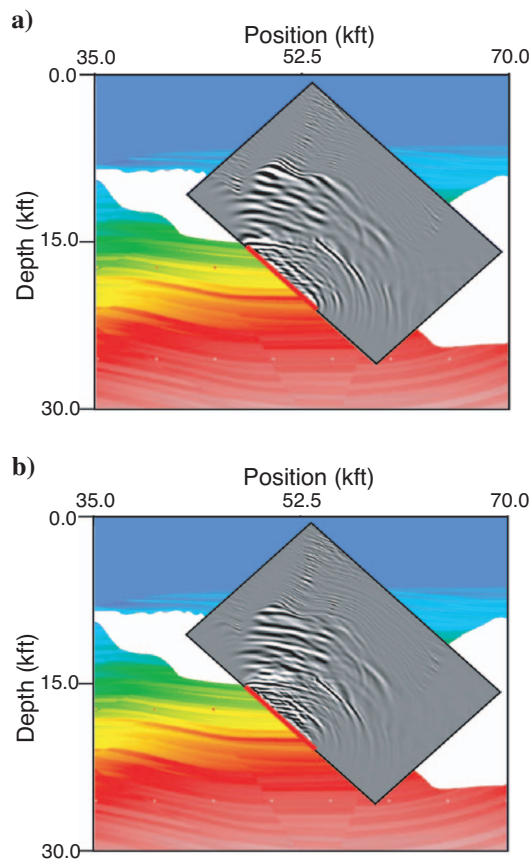

Figure 5. Images obtained from target-oriented interferometry of the Sigsbee WAW VSP data (Figure 3). Target-oriented interferometry is implemented with the wavefield separation approach described in Figure 2a, adapted to include waves that arrive from directly above the receivers. As in Figure 4, image (a) is obtained from crosscorrelation interferometry, and image (b) is obtained from deconvolution interferometry. The reflectors in these images are from single reflections reconstructed by interferometry, mostly from internal multiples. This numerical experiment is analogous to the one in Figure 1a.

array with positive shot-domain wavenumbers. Because the wavefield separation (Table 2) builds the filter u_0 from $k_r<0$, reflectors from such diving waves are not present in Figure 5.

Artifact reflectors within the salt appear more strongly in Figure 5 than in Figure 4. These can come from spurious arrivals introduced by truncation of the surface integral in interferometry (Snieder et al., 2006; Wapenaar, 2006; Vasconcelos, 2007; Vasconcelos and Snieder, 2008a). Such artifacts are understood poorly and are the subject of ongoing research.

GULF OF MEXICO SUBSALT VSP DATA

The field WAW VSP data we present here were acquired in the Gulf of Mexico and previously were used by Hornby et al. (2005) to image subsalt sediments. The experiment geometry (Figure 6) is similar to that of the numerical example discussed in the "Numerical example" section. The Gulf of Mexico data were recorded by an array of 20 three-component receivers located below the salt canopy in a well deviated from vertical approximately 40° (Figure 6a). The highest receiver is at $x = 0$ ft (0 m) and is 21,516 ft (6558 m) deep. The bottom receiver is at $x = 910$ ft (277 m) and is 23,180 ft (7065 m) deep. Receivers are 50 ft (15 m) apart within the well. Figure 6b shows the shot-receiver geometry in plane view (the N-axis points north). The 576 shots are spaced approximately 90 ft (27 m) apart. We refer to receivers in the array as receivers 1 through 20, top to bottom.

Our objective with these field data is to demonstrate the target-oriented interferometry technique as in the examples in Figures 1 and 2. Using the sources A (Figure 6b) and wavefield separation according to Figure 2a, we image the subsurface above the array, as illustrated by Figure 1a. The sources B and the wavefield separation described in Figure 2b yield an interferometric image targeted at the medium below the array, analogously to Figure 1b. With a 20-receiver array that is shorter than the array in the numerical example (see the "Numerical Example" section), interferometry generates 20 pseudoshot gathers, each recorded by 19 receivers. Because the receiver array is short (Figure 6a), the interferometric images have a much smaller aperture compared with the active-shot images from surface seismic or from the WAW VSP data (Hornby et al., 2005).

Figure 7a shows data recorded by the vertical component of motion of receiver 1 for all shots (Figure 6b). After separating waves with negative wavenumbers in the shot domain ($k_r < 0$; see Figure 2 and Table 3) and sorting the data recorded by receiver 1, we obtain the gather in Figure 7b. Keeping the positive wavenumbers in the shot gathers, ($k_r > 0$) yields the receiver gather in Figure 7c. By comparing Figure 7a and b (see arrows in the figures), we observe that the wavefield recorded at receiver 1 for $k_r < 0$ (Figure 7b) differs from the original record (Figure 7a). On the other hand, the receiver gather with only $k_r > 0$ in Figure 7c is similar to the gather in Figure 7a. The fact that the gather with $k_r > 0$ is more like the original recorded data than is the gather with $k_r < 0$ suggests that the recorded data are dominated by waves with $k_r > 0$. This is because the receiver array is below the sources and the salt, so the direct wavefield and waves scattered multiple times within the salt are recorded by the receivers as downgoing waves for which $k_r > 0$.

After wavefield separation, whose effect Figure 7 illustrates, we generated pseudoshot gathers at all receiver locations. Figures 8 and 9 show interferometric shot gathers with the pseudoshot at receiver 10. The pseudoshot gathers in Figure 8 were produced from correlation interferometry, as in equations 2 and 3. In Figure 9, we use deconvolution interferometry, as in equations 5 and 6 (Vasconcelos, 2007). We show data from receiver 10, which best illustrate the effect of target-oriented interferometry in the pseudoshot gathers because receiver 10 is in the middle of the array. For the processing of our pseudoshot gathers, we apply a Gaussian taper to the ends of the integrands (see equations 2–6) to avoid truncation artifacts (Snieder et al., 2006; Mehta et al., 2007).

The data in Figures 8a and 9a were reconstructed using all sources (Figure 6b), along with both positive and negative shot-domain wavenumbers. The pseudoshot gathers in Figures 8a and 9a contain both positive and negative wavenumbers in the pseudoshot domain. The pseudoshot in Figure 8a is dominated by positive wavenumbers because the energy in receiver data (Figure 7) is dominated by downgoing waves with $k_r > 0$. The moveout character, i.e., the pseudoshot wavenumbers, varies among the three panels in Figures 8 and 9. In figures 8b and 9b, the pseudoshot data have positive wavenumbers

for receivers that are below receiver 10 (11 through 20) and negative wavenumbers for receivers above receiver 10 (1 through 9).

This is a consequence of the choice of k_r that is used to separate the wavefield perturbations u_S (Figure 2a and Table 3). Using $k_r < 0$ for $\mathbf{r}_A$ above $\mathbf{r}_B$ yields negative pseudoshot wavenumbers for the receivers above receiver 10 (Figures 8b and 9b). Likewise, taking $k_r > 0$ for $\mathbf{r}_A$ below $\mathbf{r}_B$ yields positive pseudoshot wavenumbers at the receivers below receiver 10. The slopes in the pseudoshot gathers, thus, are controlled by the recorded shot-domain wavenumbers at the receivers in the interferometric experiment, i.e., the choice of the $\mathcal{H}_A$ filter (equation 9) in Table 3 defines the wavenumbers in Figures 8 and 9.

The data reconstructed by deconvolution interferometry (Figure 9) is impulsive, whereas pseudoshots produced by correlation inter-
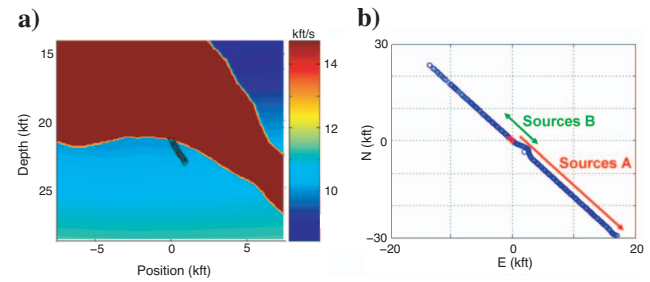

Figure 6. Geometry and acquisition of the WAW VSP field data. Panel (a) shows the velocity model derived from surface seismic. Receivers were placed in a deviated well below the salt canopy, as the black triangles in (a) indicate. Panel (b) gives a plane view of the shot-receiver acquisition geometry. Blue circles denote shot positions, and red triangles represent receiver locations. In (b), the coordinate frame is centered on the location of the shallowest receiver. N is northward distance; E is eastward distance. The orientation of the velocity profile in (a) coincides with that of the WAW line in (b). The lateral distance in (a) also is measured with respect to the location of the shallowest receiver, along the direction of the acquisition plane. The arrows in (b) indicate which sources are used for controlling illumination of interferometric data. Sources A (red) correspond to sources over σ_1 in the experiment in Figure 1a. Sources B (green) contribute to imaging below the array (source over σ_2, Figure 2b).
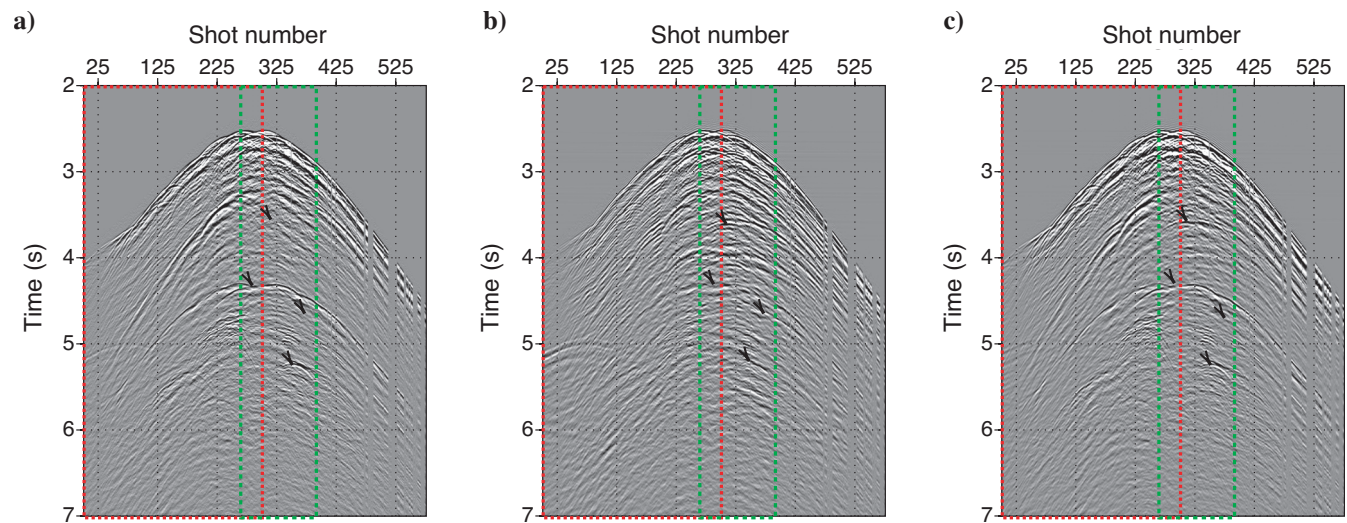

Figure 7. The effect of wavefield separation on receiver gathers from field data. Panel (a) shows the original data recorded at receiver 1 (shallowest receiver in Figure 6a). The receiver gather in panel (b) contains only waves with $k_r < 0$ (see Figure 2). The data in (c) come from the positive wavenumbers in the shot domain ($k_r > 0$). Black arrows highlight portions of data for which wavefield separation has a visible effect. Data that correspond to sources A (Figure 6b; Table 3) are outlined in red, whereas data excited by sources B are outlined in green.

ferometry (Figure 8) have the imprint of the autocorrelation of the sourcewavelet (Vasconcelos and Snieder, 2008a; Wapenaar and Fokkema, 2006). In our case, the wavefield in the field data is generated by marine air-gun sources. Hence, the data in Figure 8 are the averaged autocorrelation of the air-gun source-time function convolved with the reflection response (equations 2 and 3). However, the data in Figure 9 do not contain the signature of the air-gun source (equations 5 and 3). Mehta et al. (2007a) also observe the presence of this source autocorrelation in interferometry of OBC data. In that case, the autocorrelation excitation is removed with an independent estimate of the air-gun source function. Here we rely on deconvolution interferometry (Vasconcelos, 2007) to reconstruct impulsive pseudoshot data (Figure 9) because an estimate of the air-gun autocorrelation was not available.

We migrate all pseudoshot gathers using shot-profile reverse time migration (Baysal et al., 1983). Each panel in Figure 10 is the result of stacking the migrated images from pseudoshots placed at every receiver in the array. In other words, the Figure 10 images are the result of migrating all of the pseudosources (there is one for every receiver in the array; Figure 6a). Table 3 describes the processing for and meaning of the images in Figure 10.

Although the pseudosources that result in Figure 10b and e radiate energy upward ("Radiation" column, Table 3) the salt above the array reflects a portion of the radiated energy downward. This explains the image artifacts below the receiver array in Figure 10b and e. Furthermore, because wavefield separation is done using f-k filtering, the small aperture of the array might introduce a wavenumber bias during wavefield separation, i.e., wavenumber sensitivity decreases with decreasing array size. This bias can produce crosstalk (Wapenaar and Fokkema, 2006) between waves propagating in different directions, which contributes to energy below the array in Figure 10b and e. Figure 10c and f are from interferometric sources that radiate energy downward (Table 3), which results in images that have most of the energy concentrated below the array. Figure 10a and d are the result of migrations using the velocity model in Figure 6a.

We removed the top of salt (replaced sediment above the salt with salt velocity) in the top right corner of Figure 6a to generate the images in Figure 10b-e. The absence of the salt top in the velocity model ensures that top-of-salt reflectors are not artifacts introduced by the salt/sediment contrast in the model. The influence of the bottom-salt velocity contrast can be seen in all Figure 10 images whose reflectors in the lower right quadrant terminate abruptly. Image aperture in Figure 10 is controlled by the geometry of the receiver array because receivers act as both sources and receivers in interferometry. Thus, because the array is relatively small (Figure 6a), the circular patterns in the images are artifacts of the migration operator where the subsurface is not sampled by specular reflections.

To facilitate interpretation of the interferometric images in Figure 10c and e, I isolate the portions of the subsurface that are sampled physically by the images in Figure 11. For spatial reference, we superpose the interferometric images over the velocity model estimated from surface seismic data (Figure 11 background) and indicate the receiver-array position (blue line). The image from deconvolution-based target-oriented interferometry (Figure 11b) recovers the reflector that corresponds to the top of salt inferred from surface seismic. This reflector is not visible in Figures 11a and 10c. Wavefield separation (see Table 3) is necessary to separate the events that illuminate the top-of-salt reflector in Figure 11b. Although Figure 11c also is a product of target-oriented interferometry, the top-of-salt reflector is obscured by autocorrelation of the air-gun source function mapped onto the image. The image in Figure 11b comes from deconvolution interferometry, in which migration of pseudoshots results in an impulsive image (Vasconcelos and Snieder, 2008a, 2008b).

DISCUSSION

We present an interferometric method that generates pseudosources that radiate energy in a predetermined direction. The direction of radiated energy is controlled by the choice of wavefields u_0 and u_S used in interferometry (equations 2–6). In particular, here we

Table 3. Processing that leads to the images in Figure 10.[6]

	u_0	u_S	$\mathcal{H}_A$	$\mathcal{H}_B$	Sources	Method	Radiation
Figure 10a	Not separated	Not separated	Not applicable	Not applicable	All	Correlation (equation 2)	Not controlled*
Figure 10b	Upgoing (e.g.,primaries)	Downgoing (e.g.,multiples)	$k_r>0$; $\mathbf{r}_A$ below $\mathbf{r}_B$ $k_r<0$; $\mathbf{r}_A$ above $\mathbf{r}_B$	$k_r<0$	Sources A (Figures 6b and 7)	Correlation (equation 3)	↗
Figure 10c	Downgoing (e.g., direct-wave)	Upgoing (e.g., primaries)	$k_r<0$	$k_r>0$	Sources B (Figures 6b and 7)	Correlation (equation 3)	↓
Figure 10d	Not separated	Not separated	Not applicable	Not applicable	All	Deconvolution (equation 5)	Not controlled*
Figure 10e	Upgoing (e.g., primaries)	Downgoing (e.g.,multiples)	$k_r>0$; $\mathbf{r}_A$ below $\mathbf{r}_B$ $k_r<0$; $\mathbf{r}_A$ above $\mathbf{r}_B$	$k_r<0$	Sources A (Figures 6b and 7)	Deconvolution (equation 6)	↗
Figure 10f	Downgoing (e.g.,direct-wave)	Upgoing (e.g.,primaries)	$k_r<0$	$k_r>0$	Sources B (Figures 6b and 7)	Deconvolution (equation 6)	↓

[3]Column-heading and asterisk meanings are as for Table 2. Arrows indicating the direction of pseudosource radiation are oriented with respect to the receiver array (Figures 6 and 11).

use a wavenumber-filtering method (equations 8 and 9) for wave-field separation. In the absence of dual-field measurements (see below), it also is possible to use more sophisticated methods of directional decomposition, e.g., curvelets (Candès, 2006; Douma and de Hoop, 2007). Note that wavenumber filtering, along with source selection (as used here), allows discrimination between any propagation directions except that which is perpendicular to the receiver array. This is why the wavenumber method is useful for the deviated-well geometries we show here but is not ideal for horizontal receiver arrays.

Other wavefield-separation methods can be used in interferometry (Vasconcelos and Snieder, 2008a). To image below a borehole receiver array, Bakulin and Calvert (2006) use muting to separate downgoing direct waves from the remainder of the data. This method can be used to reconstruct all upgoing reflections but not to reconstruct only downgoing reflections. Mehta, et al. (2007a) use dual-field information to separate upgoing from downgoing waves.

In principle, full dual-field measurements (pressure and three-component particle velocity) can be used to select waves propagating in any desired direction. For example, a *p-z* (pressure and vertical velocity component) summation method (Mehta et al., 2007a) distinguishes upgoing from downgoing waves, whereas a *p*-*x* summation (pressure and horizontal velocity component) tells which way waves propagate horizontally. Thus, proper combinations of velocity components and pressure can be used to select waves in any propagation direction within an acoustic medium. However, in practice, dual-field separation based on pressure and velocity measurements becomes approximate in a heterogeneous, elastic earth.

Another possibility is to combine wavenumber separation with dual-sensor techniques, which in principle could enable generation of pseudo-sources that can radiate energy in any desired direction.

In the example from the Sigsbee salt model, seismic interferometry with no wavefield separation yields an image of the salt body that is well defined in the dipping salt flanks. These reflectors are sampled mainly by diving waves, as in the numerical experiment by Willis et al. (2006). The images obtained from target-oriented interferometry recover the reflectors at the top and base of salt located immediately above the receiver array. They also recover a portion of the subsalt sediment structure that cannot be retrieved by interferometry of the full recorded wavefields.

These images also present artifacts that might be caused by truncation of the surface integral in interferometry. Truncation of the surface integral (Wapenaar, 2006; Vasconcelos and Snieder, 2008a) can lead to a nonzero error in wavefield-reconstructed interferometry (Wapenaar, 2006; Vasconcelos and Snieder, 2008a). This might cause amplitude and phase distortions (Wapenaar, 2006; Vasconcelos, 2007) and can introduce spurious arrivals (Snieder et al., 2006; Vasconcelos and Snieder, 2008a). The effect of sur-

face truncation has not been assessed yet in detail because the effects of surface truncation are model dependent.

Our interferometric procedure is approximate also because it neglects a volume integral of the medium perturbations required by the interferometry method in perturbed media (Vasconcelos, 2007). This approximation leads to the reconstruction of interferometric shots that are kinematically correct but have distorted amplitudes. Therefore, target-oriented interferometry as presented here is suitable mostly for structural imaging.

Using field WAW VSP data acquired in the Gulf of Mexico (Hornby et al., 2005), we illustrate that the choice of shot-domain wavenumbers at receivers that record interferometric data controls wavenumbers in the pseudoshot gathers. Because the air-gun excitation in the field data is not impulsive, we rely on deconvolution interferometry after source summation (Vasconcelos, 2007) to reconstruct impulsive pseudoshot data. When an independent estimate of air-gun autocorrelation is available, it can be deconvolved directly from correlation-based pseudoshot gathers (Mehta et al., 2007a).
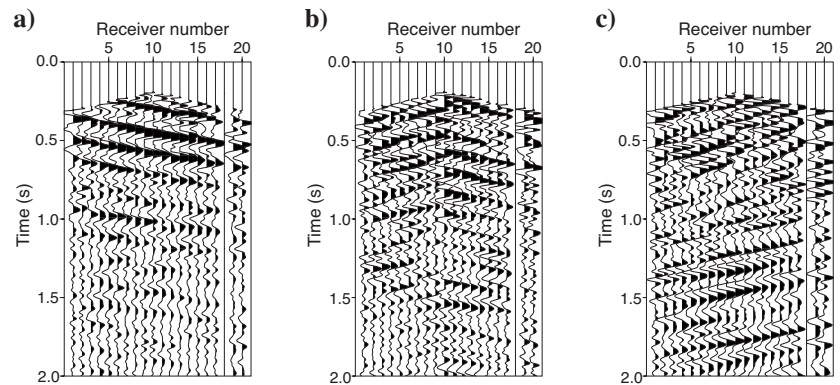

Figure 8. Interferometric shot gathers with pseudoshot at receiver 10, reconstructed with correlation interferometry. The pseudoshot gather in (a) is the result of correlating the full wavefields from all sources (Figure 6b). Separating the wavefield according to Figure 2a and using data from sources A for interferometry yields the pseudoshot gather in (b). Panel (c) comes from interferometry of data from sources B after wavefield separation, as in Figure 2b. All data are muted for removal of the direct wave.
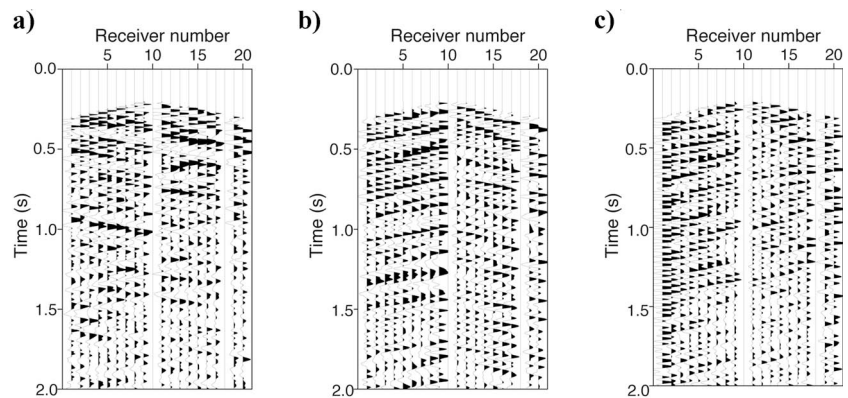

Figure 9. Pseudoshot gathers from deconvolution interferometry. The input data in panels (a), (b), and (c) are the same as in Figure 8a-c, respectively. The data in (a) are reconstructed from the full wavefield from all sources (Figure 6b). Sources A (Figure 6b) and wavefield separation according to Figure 2a were used to obtain the gather in (b). The data in (c) come from applying wavefield separation in Figure 2b to sources B and performing deconvolution interferometry.

a)

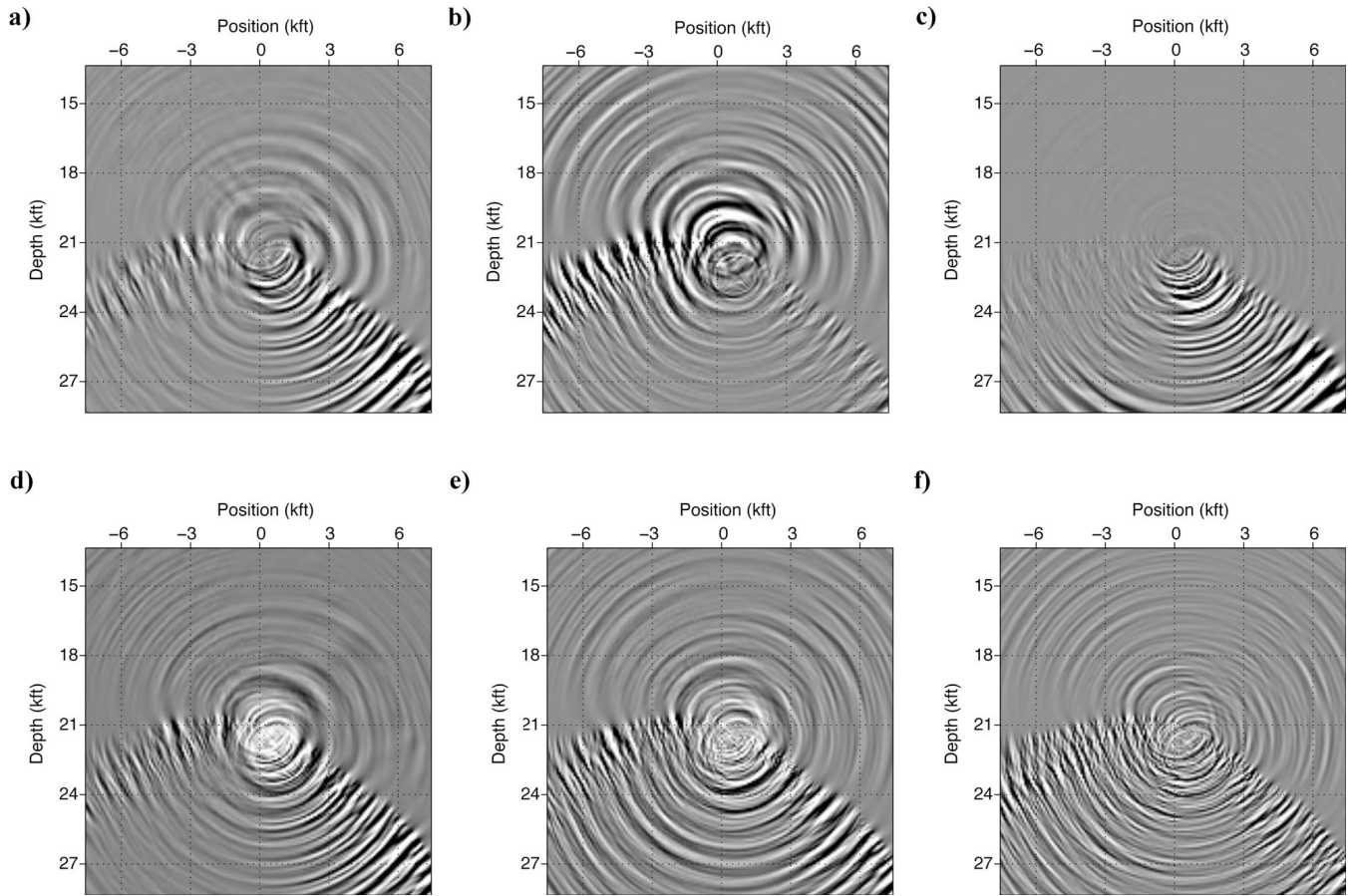Position (kft)

b)

Position (kft)

c)

Position (kft)

Figure 10. Comparison of images after reverse-time migration, with and without target-oriented interferometry. Table 3 describes the input data and interferometry method used in each image. The images are the result of stacking the shot-profile migrations of all pseudoshots. Images (a) and (d) correspond to use of all sources and the full wavefield for interferometry. Images (b) and (e) are from pseudosources that radiate energy upward (Table 3). Images (c) and (f) are the result of reverse-time migration of pseudosources designed to radiate energy downward (Table 3). Images (a), (b), and (c) are from correlation interferometry. Images (d), (e), and (f) were obtained using deconvolution interferometry. All images correspond to the same subsurface portion shown by the model in Figure 6a. Image aperture is controlled by geometry of the receiver array (Figure 6a).

a)

Position (kft)
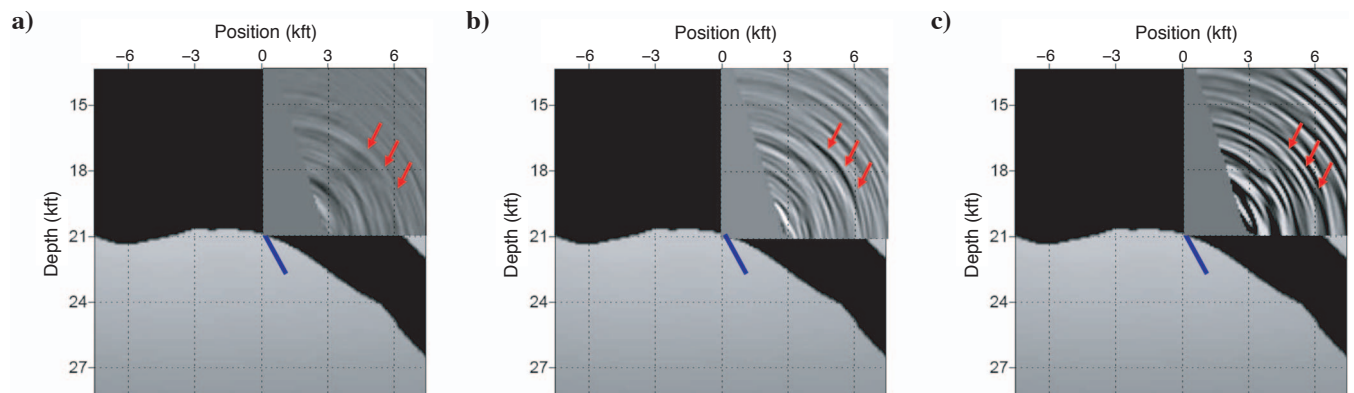
b)

Position (kft)

c)

Position (kft)

Figure 11. Interferometric images of the upper right portion of the subsurface above the receiver array (see Figure 6a). The images are superimposed on the velocity model that was estimated from surface seismic data. The blue line represents the receiver array. Image (a) was extracted from Figure 10d and corresponds to use of the full wavefield from all sources in seismic interferometry. Images (b) and (c) target reflectors above the array (Figures 1a and 2a). Images (a) and (b) are from deconvolution interferometry (extracted from Figure 10d and e, respectively). Image (c) is from correlation interferometry (Figure 10b). Red arrows indicate the top of salt, interpreted from surface seismic (Figure 6a).

Using wavefield separation to design pseudoshots that radiate energy upward, we image the top of salt from the receiver array using recorded internal multiples. This top-of-salt reflector is not reproduced by the image from interferometry of the full recorded wavefields. Furthermore, we use the subsalt VSP data to demonstrate how interferometry can be manipulated to target the subsurface below the array (see also Bakulin and Calvert, 2006). This application is the same as in the virtual-source method (Bakulin and Calvert, 2006; Mehta et al., 2007a), but our wavenumber-filtering approach is different from that presented by Bakulin and Calvert (2006) and by Mehta et al. (2007a).

We show examples of 2D interferometric imaging. As with the more standard active-shot VSP imaging techniques, the interferometric imaging of single-well 3D VSP data can be problematic around highly complex 3D structures. This happens because, regardless of how many receivers are placed in a well, there usually is no way to know which way the waves propagate in the plane to which the well is perpendicular. In that case, wavefield separation by wavenumbers no longer is accurate. Resolving directions in 3D VSP data requires either data that were recorded in multidirectional wells and/or requires dual-field records (using polarization information along with wavenumbers).

The interferometric experiments presented in this paper are not necessarily restricted to active-shot VSP experiments and P-wave imaging. The same experiments are possible in the context of passive seismic measurements (Draganov et al., 2006) or in interferometric imaging of drill-bit noise records (Poletto and Miranda, 2004; Vasconcelos and Snieder, 2008b). Wapenaar (2004), Draganov et al. (2006), and Vasconcelos and Snieder (2008b) present methodologies to recover elastic pseudoshot records using seismic interferometry. Likewise, target-oriented interferometry can be designed to recover multicomponent subsalt pseudoshot records. Such records, along with surface seismic data, can help improve the understanding of local physical structure in subsalt environments. This understanding might take the form of more realistic models of the subsalt velocity field that incorporate anisotropy and lateral parameter variations.

It might be worthwhile to design VSP acquisitions for specific interferometry applications, such as the one presented here or the one in Bakulin and Calvert (2006). In particular, we note two important points to consider when designing an interferometric VSP experiment. First, it is important to use long receiver arrays and long recording times in acquiring data to be used for interferometry. As in the Sigsbee numerical example, long receiver arrays can help in obtaining interferometric images with a wide image aperture. Every receiver added to an array contributes both a source and a receiver to the interferometry experiment. The poor image aperture in our Gulf of Mexico example is caused precisely by use of a small downhole receiver array. Second, it would be a great advantage to record dual-field data, e.g., both pressure and particle-velocity fields, in VSP acquisition in zones of high structural complexity in three dimensions.

CONCLUSION

We present an interferometric technique based on wavefield separation in the shot domain that targets the reconstruction of specific arrivals in the interferometric shot gathers. This target-oriented interferometry technique can be used to reconstruct single-reflected waves from internal multiples. Such a reconstruction can be applied, for example, to the imaging of subsalt features above receiver arrays in subsalt in WAW VSP experiments.

Our target-oriented interferometry technique is based on two-way representation theorems derived for perturbed acoustic media. Application of the technique consists of manipulating the recorded data to separate unperturbed waves at the receiver that acts as a pseudo-source and to separate wavefield perturbations at receivers that record the interferometric experiment. We separate these wavefields according to the directions of the waves coming in to a given receiver, i.e., according to the shot-domain wavenumber. This procedure can be tailored to generate pseudosources that radiate energy in any desired direction.

REFERENCES

Bakulin, A., and R. Calvert, 2004, Virtual source: New method for imaging and 4D below complex overburden: 74th Annual International Meeting, SEG, Expanded Abstracts, 2477–2480.
——, 2006, The virtual-source method: Theory and case study: Geophysics, **71**, no. 4, SI139–SI150.
Baysal, E., D. D Kosloff, and J. W. C. Sherwood, 1983, Reverse time migration: Geophysics, **48**, 1514–1524.
Berkhout, A. J., and D. J. Verschuur, 2006, Imaging of multiple reflections: Geophysics, **71**, no. 4, SI209–SI220.
Candès, E., L. Demanet, D. Donoho, and L. Ying, 2006, Fast discrete curvelet transforms: Multiscale Modeling and Simulation, **5**, 861–899.
Curtis, A., P. Gerstoft, H. Sato, R. Snieder, and K. Wapenaar, 2006, Seismic interferometry — Turning noise into signal: The Leading Edge, **25**, 1082–1092.
Draganov, D., K. Wapenaar, and J. Thorbecke, 2006, Seismic interferometry: Reconstructing the earth's reflection response: Geophysics, **71**, no. 4, SI61–SI70.
Douma, H., and M. V. de Hoop, 2007, Leading-order seismic imaging using curvelets: Geophysics, **72**, no. 6, S231–S248.
Grech, M. G. K., D. C. Lawton, and S. Cheadle, 2003, Integrated prestack depth migration of vertical seismic profile and surface seismic data from the Rocky Mountain Foothills of southern Alberta, Canada: Geophysics, **68**, 1782–1791.
Hargreaves, N., 2006, Surface multiple attenuation in shallow water and the construction of primaries from multiples: 76th Annual International Meeting, SEG, Expanded Abstracts, 2689–2693.
Hornby, B., T. Fitzpatrick, F. Rollins, H. Sugianto, and C. Regone, 2005, 3D VSP used to image near complex salt structure in the deep water Gulf of Mexico: 67th Conference & Exhibition, EAGE, Extended Abstracts, E022.
Kessinger, W., 1992, Extended split-step Fourier migration: 62nd Annual International Meeting, SEG, Expanded Abstracts, 917–920.
Larose, E., L. Margerin, A. Derode, B. van Tiggelen, M. Campillo, N. Shapiro, A. Paul, L. Stehly, and M. Tanter, 2006, Correlation of random wavefields: An interdisciplinary review: Geophysics, **71**, no. 4, SI11–SI21.
Lobkis, O. I., and R. L. Weaver, 2001, On the emergence of the Green's function in the correlations of a diffuse field: Journal of the Acoustical Society of America, **110**, 3011–3017.
Mehta, K., A. Bakulin, J. Sheiman, R. Calvert, and R. Snieder, 2007a, Improving the virtual-source method by wavefield separation: Geophysics, **72**, V79–V86.
Mehta, K., R. Snieder, and V. Graizer, 2007b, Extraction of near-surface properties for a lossy layered medium using the propagator matrix: Geophysical Journal International, **169**, 271–280.
Poletto, F. B., and F. Miranda, 2004, Seismic while drilling: Fundamentals of drill-bit seismic for exploration: Elsevier.
Schuster, G. T., F. Followill, L. J Katz, J. Yu, and Z. Liu, 2004, Autocorrelo-

gram migration: Theory: Geophysics, **68**, 1685–1694.

Schuster, G. T., and M. Zhou, 2006, A theoretical overview of model-based and correlation-based redatuming methods: Geophysics, **71**, no. 4, SI103–SI110.

Snieder, R., and E. Şafak, 2006, Extracting the building response using seismic interferometry: theory and application to the Millikan library in Pasadena, California: Bulletin of the Seismological Society of America, **96**, 586–598.

Snieder, R., K. Wapenaar, and K. Larner, 2006, Spurious multiples in seismic interferometry of primaries: Geophysics, **71**, no. 4, SI111–SI124.

Vasconcelos, I., 2007, Interferometry in perturbed media: Ph.D. dissertation, Colorado School of Mines.

Vasconcelos, I., and R. Snieder, 2008a, Interferometry by deconvolution: Part 1 — Theory for acoustic waves and numerical examples: Geophysics, **73**, no. 3, S115–128.

——, 2008b, Interferometry by deconvolution: Part 2 — Theory for elastic waves and application to drill-bit seismic imaging: Geophysics, **73**, no. 3, S129–141.

Vasconcelos, I., S. T. Taylor, R. Snieder, J. A. Chavarria, P. Sava, and P. Malin, 2007, Broadside interferometric and reverse-time imaging of the San Andreas Fault at depth: 77th Annual International Meeting, SEG, Expanded Abstracts, 26, 2175–2179.

Wapenaar, K., 2004, Retrieving the elastodynamic Green's function of an arbitrary inhomogeneous medium by cross correlation: Physical Review Letters, **93**, 254301.

——, 2006, Green's function retrieval by cross-correlation in case of one-sided illumination: Geophysical Research Letters, **33**, L19304.

Wapenaar, K., and J. Fokkema, 2006, Green's function representations for seismic interferometry: Geophysics, **71**, no. 4, SI33–SI46.

Wapenaar, K., J. Thorbecke, and D. Draganov, 2004, Relations between reflection and transmission responses of three-dimensional inhomogeneous media: Geophysical Journal International, **156**, 179–194.

Weglein, A. B., F. V. Araújo, P. M. Carvalho, R. H. Stolt, K. H. Matson, R. T. Coates, D. Corrigan, D. J. Foster, S. A. Shaw, and H. Zhang, 2003, Inverse scattering series and seismic exploration: Inverse Problems, **19**, R27–R83.

Weglein, A. B., B. G. Nita, K. A. Innanen, E. Otnes, S. A. Shaw, F. Liu, H. Zhang, A. C. Ramírez, J. Zhang, G. L. Pavlis, and C. Fan, 2006, Using the inverse scattering series to predict the wavefield at depth and the transmitted wavefield without an assumption about the phase of the measured reflection data or back propagation in the overburden: Geophysics, **71**, no. 4, SI125–SI137.

Willis, M. E., R. Lu, X. Campman, M. N Toksöz, Y. Zhang, and M. V. de Hoop, 2006, A novel application of time-reversed acoustics: Salt-dome flank imaging using walkaway VSP surveys: Geophysics, **71**, no. 2, A7–A11.

Xiao, X., M. Zhou, and G. T. Schuster, 2006, Salt-flank delineation by interferometric imaging of transmitted P- to S-waves: Geophysics, **71**, no. 4, SI197–SI207.